




# Tailoring graphitic nanostructures in hard carbons as anode materials achieving efficient and ultrafast sodium storage

Yuxiang Chen<sup>1</sup>, Jie Li<sup>1</sup>, Yanqing Lai<sup>1</sup>, Junming Li<sup>1</sup>, and Zhian Zhang<sup>1,2,\*</sup> 

<sup>1</sup>School of Metallurgy and Environment, Central South University, Changsha 410083, China

<sup>2</sup>Engineering Research Center of High Performance Battery Materials and Devices, Research Institute of Central South University in Shenzhen, Shenzhen 518057, China

Received: 22 December 2017

Accepted: 3 April 2018

Published online:  
12 April 2018

© Springer Science+Business  
Media, LLC, part of Springer  
Nature 2018

## ABSTRACT

Hard carbons appear to be promising anode candidates in high-performance sodium-ion batteries (SIBs) for large-scale stationary energy storage due to their large interlayer distance and amorphous structure, which facilitate sodium ions insertion/desertion. However, several major hurdles to address are poor rate performances and the low initial coulombic efficiency (ICE). Herein, a facile strategy to tailor hard carbons with graphitic nanostructures and rational specific surface area is proposed to improve sodium storage. Resin-derived carbon nanobroccolis (CNB) with in situ decorated graphitic nanostructures have been successfully synthesized by self-assembly and low-temperature catalytic carbonization process. As a result, attribute to in situ tailored graphitic nanostructures in hard carbons and rational specific surface area, CNB electrodes possess less charge transfer resistance and excellent sodium ions diffusion kinetics and successfully achieve fast and efficient sodium storage. When used as anode for sodium-ion batteries, CNB electrodes exhibit excellent high-rate capability of 137 mAh g<sup>-1</sup> at 1000 mA g<sup>-1</sup> and enhanced ICE of 52.6%. Our strategy reported here opens a door to design high-performance carbon anode materials for SIBs particularly focusing on efficient sodium ions storage and fast sodium ions diffusion.

## Introduction

In the last three decades, the lithium-ion batteries (LIBs) have been spreading from portable electronic devices to vehicle electrification and power grid. However, the limits of the uneven global distribution

and natural abundance of lithium-containing precursors present unavoidable challenges to industry. As one type of the most promising candidates, sodium-ion batteries (SIBs) have drawn significant attention due to the low-cost, ubiquitous and widespread reserves of sodium mineral salts.

Address correspondence to E-mail: zhangzhian@csu.edu.cn

Advances in electrode materials which undertake the electrochemically insertion/desertion of sodium ions are undoubtedly fundamental and important for the improvement of battery performance. Enormous efforts have been dedicated to the progress of high-performance anode materials, because, unlike LIBs, the electrochemical sodiation/desodiation capacity of graphite is as low as 35 mAh g<sup>-1</sup>. More problematically, the formation of graphite intercalation compounds is energetically unfavorable in SIBs [1, 2].

Recently, intensive research efforts have focused on developing SIBs anode candidates including carbon nanowires [3], carbon nanosheets [4], carbon nanofibers [5], carbon nanoparticles [6, 7] and so on [8, 9]. Among various carbonaceous materials, hard carbons are considered as promising anode materials for SIBs because of their large interlayer distances and amorphous structures, which facilitates sodium ions insertion and desertion [10]. Dahn's group [11] first reported hard carbon as the anode material for SIBs, exhibiting a high specific capacity of 280 mAh g<sup>-1</sup> at 20 mA g<sup>-1</sup>. Subsequently, hard carbons derived from glucose [12], shaddock peel [13], pyrolyzed anthracite [14], cotton [15], wood [16], filter paper [17] all exhibit superior specific capacity. The specific capacities of hard carbons for the first discharge cycle were somewhat higher than 300 mAh g<sup>-1</sup> due to the large interlayer spacing and large electrode/electrolyte contact area and efficient and continuous electron transport of the porous carbon structure. Unfortunately and inevitably, owing to the amorphous structure, the electronic conductivity of hard carbons usually is relatively low and leads to an unfavorable rate capability. Meanwhile, the high specific surface area induces the formation of vast solid electrolyte interphase layer and then results in a low initial coulombic efficiency as well as poor cyclic stability [6, 8, 18, 19].

Generally, increasing the graphitization degree of amorphous carbons by high-temperature heat treatment (> 1300 °C) could improve their electronic conductivity, coulombic efficiency [8] and rate capability [15]. The graphite-like micro-crystallites increase evidently with the increase in carbonization temperature due to the reduction in some defects and heteroatoms as well as the rearrangement of carbon atoms [20]. Nevertheless, high-temperature carbonization unavoidably destroys the porous structure, shrinks the interlayer spacing and weakens the ionic conductivity, and then leads to a low specific

capacity of hard carbon, especially at high discharge current density. As a result, only 98 mAh g<sup>-1</sup> remained at 500 mA g<sup>-1</sup> for corn cob-derived hard carbon [20] and 85 mA h g<sup>-1</sup> remained at 900 mA g<sup>-1</sup> for templated carbon [21]. Therefore, it is extremely important to develop novel and efficient method to improve the electrochemical performance for hard carbons in SIBs.

Motivated by these considerations, a facile and scalable method was proposed for the design and preparation of carbon nanobroccoli tailored with porous expanded graphitic nanostructures (CNB) via a combined process of chemical polymerization and low-temperature catalytic carbonization. In this work, lignin–resorcinol–formaldehyde (LRF) hydrogel was achieved by chemical polymerization in FeCl<sub>3</sub> concentrated solution. Benefiting from the template and catalytic graphitization of Fe species, broccoli-like morphology hard carbons were in situ tailored with porous high graphitic nanostructure, possessing excellent electronic conductivity, rational accessible surface area, strong structural stability, less charge transfer resistance and excellent sodium ions diffusion kinetics. Compared with traditional carbonaceous monolithic material, the specific capacity of CNB electrodes was improved from 166 to 337 mAh g<sup>-1</sup> at 50 mA g<sup>-1</sup>; in addition, the initial coulombic efficiency (ICE) was greatly improved from 29.0 to 52.6%. Meanwhile, CNB as anode materials demonstrated superior high current cycling stability at 1000 mA g<sup>-1</sup>, and 137 mAh g<sup>-1</sup> remained after 1000 cycles. Our strategy reported here opens a door to the design and tailoring of amorphous carbons with excellent electronic conductivity and less specific surface area for efficient and fast energy storage.

## Results and discussion

The synthesis of electrode materials as well as the construction of CNB by a two-step procedure of in situ polymerization and catalytic carbonization is presented in Fig. 1. Detailed synthetic procedure was described in experimental section. Resorcinol–formaldehyde resins are artificially synthesized flexible precursors with low cost leading to high-purity carbons with precise control of chemical properties [22]. The lignin is an abundant carbon-rich biopolymer comprising three different phenolic alcohol

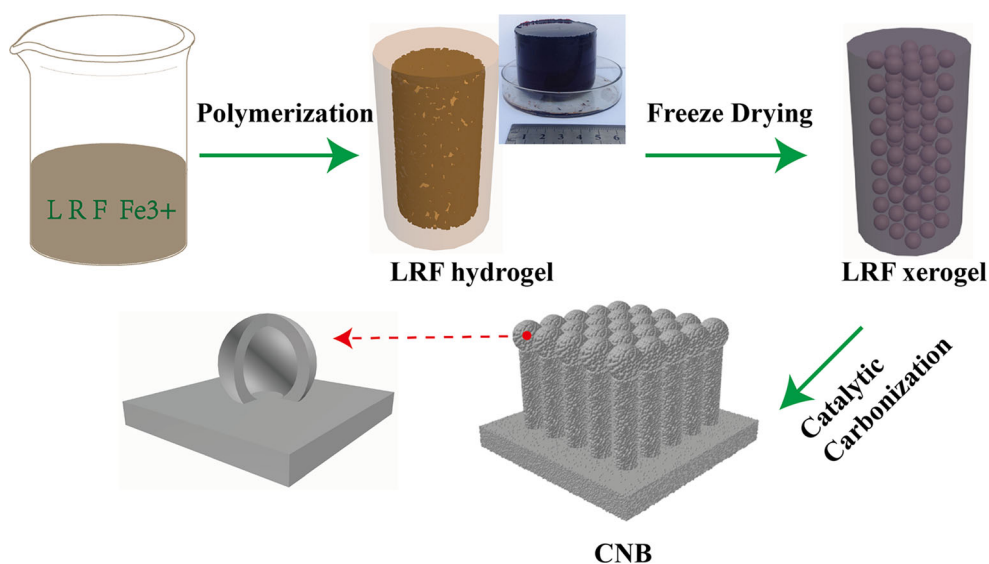


**Figure 1** Schematic illustration of the synthesis procedure of CNB.

monomers, which can be used to partly replace the use of resorcinol. The chelation effect [23] of  $\text{Fe}^{3+}$  with polymer monomers via liquid-phase method [24] can improve the dispersion of metal catalysts into carbon precursor units, yielding a better catalytic effect. The LRF–KCl was set as reference. Firstly, phenolic alcohol nanomers in resorcinol and lignin reacted with formaldehyde to form hydroxymethyl derivatives, methylene and methylene ether bridged gel networks [25]. Secondly, after freezing drying, abundant ultrafine  $\text{FeCl}_3$  particles could be highly dispersed in LRF xerogel. Thirdly, thermal decomposition, chemical decomposition and recombination reactions of the resin occurred upon heat treatment [26]. At low temperature,  $\text{FeCl}_3$  particles could be engaged as hard template [27]. At high temperature, the Fe nanoparticles are formed and uniformly decorated into carbon matrix by in situ carbon-thermal reduction in the decomposition residues of ferric chloride. Fe species possess strong catalytic effect of graphitization [28]. Benefiting from the migration and accumulation of Fe species in the matrix [2], expanded nanographite in situ formed in the carbon matrix and generated ordered structures around the Fe species [28]. Lastly, when Fe species were etched away, graphitic carbon nanostructures were left highly dispersed in the hard carbon matrix [29].

The tailored ordered graphitic structures into hard carbons were confirmed by X-ray diffraction as shown in Fig. 2a. CNB and CM exhibit broad peaks center at around  $25^\circ$  and  $23^\circ$ , corresponding to the

(002) graphitic structure diffraction. The (002) peak position of CNB shifts to a higher angle indicating the tiny decrease in ( $d_{002}$ ). With the catalytic graphitization of Fe species, part of amorphous carbon converted to expanded graphite [27].

Raman spectroscopy can be used to efficiently reveal the defects level and degrees of graphitization of carbon materials [30]. For CNB and CM, two obvious peaks are identified in the Raman spectrums (Fig. 2b) at  $1320$  and  $1590\text{ cm}^{-1}$ , corresponding to the D band and G band of carbons, respectively. As demonstrated in Fig. 2b, compared with CM (1.02), the peak intensity ratio  $I_D/I_G$  of CNB (0.93) reflects an increase in the graphitic degree in CNB, which indicated the catalytic graphitization of Fe species [29]. For carbons, the graphitic crystallite size in plane  $L_a(\text{nm})$  can be quantified based on Eq. (1) by the peak intensity ratio:

$$L_a = 2.4 \times 10^{-10} \lambda^4 \frac{I_G}{I_D} \quad (1)$$

where  $I$  was the integrated intensity of the corresponding band and  $\lambda$  was the laser energy in nanometers [30]. Based on the Raman spectra of CNB, CM and Eq. (1), the graphitic domain sizes of CNB and CM were approximately 20.6 and 18.7 nm, respectively, which further indicates the development of local short-range ordered structure in CNB.

Scanning electron microscopy (SEM) characterization was performed to observe the surface morphology of carbon nanobroccolis. Figure 3a exhibits the

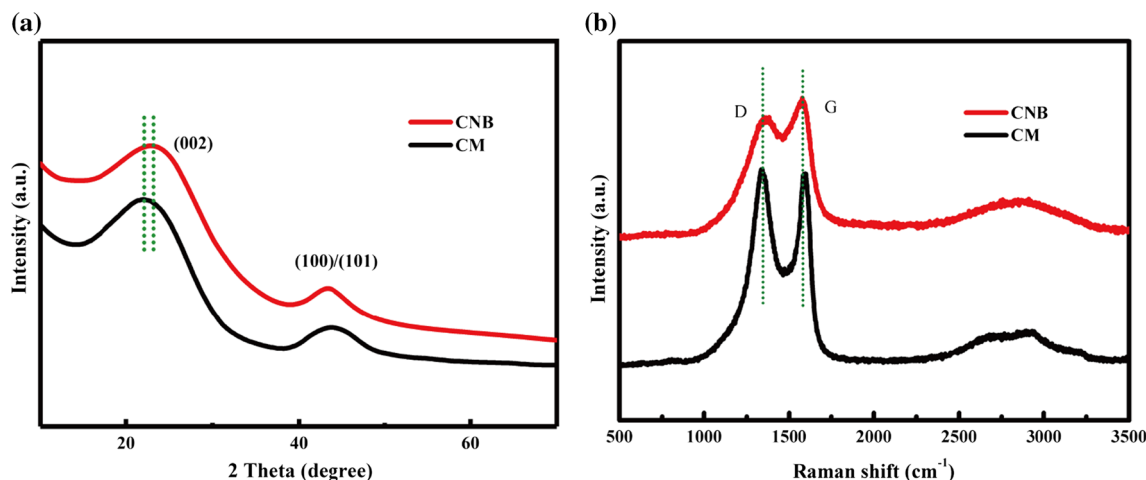


**Figure 2** a XRD patterns of CNB and CM, b Raman spectra of CNB and CM.

uniform dispersion of carbon particles with 200 nm diameter on the branch. As shown in Fig. 3b, different from the carbon nanosheets in Fig. S1a, carbon blocks with rough surface were surrounded by abundant cross-linked depressions. The unique structure is in favor to the contact and madeaction for active materials and electrolyte [6]. As observed in Fig. 3c, typical amorphous structures and graphitic structures can be clearly visible in the carbon matrix (region 1) and on the outskirts of hard carbon (region 2,3). As shown in Fig. 3d (the enlarged drawing of region 1), amorphous structures fill the whole screen, indicating that the resorcinol–formaldehyde resins are typical applicable hard carbon precursors. Benefit from the catalytic graphitization effect of Fe species, some carbon layers shift and oxygen-containing functional groups decompose. In contrast to region 1, ordered graphitic structures can be well observed by the alternating bright and dark contrast in region 2 (Fig. 3e). Amazingly, as clearly shown in Fig. 3f (the details drawing of region 3), graphitic structures are closely anchored on the amorphous carbon matrix.

Especially, ordered-disordered cross-linking in region 4 convincingly demonstrates that in situ formed ordered carbon layers are deeply rooted in these amorphous carbon structures. Those are consistent with the results in crystal structures. Observations of surface morphology provide strong evidences for the successfully tailoring. Different from CNB, typical amorphous structure can be seen in CM (as shown in Fig. S1b). It is well established that the in situ formed graphitic structures can improve the electrical conductivity of hard carbon,

provide sufficient electrons transfer for the  $\text{Na}^+$  intercalation and extraction process, reduce the charge transfer impedance and hence improve the rate capability of the hybrid [19, 31]. In addition, the average interlayer spacing is measured to be 0.347 nm for the ordered graphitic carbon layers due to the residual oxygen-containing groups [1], which is still larger than graphite (0.335 nm).

For detailed analysis of the porosity differences between CNB and CM,  $\text{N}_2$  sorption measurements based on BET model were implemented (Fig. 4a). The pore structures of porous carbon were tested by typical nitrogen adsorption/desorption isotherms at 77 K (Fig. S2a). The specific surface area for CNB was  $74.5 \text{ m}^2 \text{ g}^{-1}$ , considerably below that of CM ( $768.5 \text{ m}^2 \text{ g}^{-1}$ ). Distinct increase in  $\text{N}_2$  uptake of CM at low pressure from 0 to 0.3 ( $P/P_0$ ) indicated a good deal of micropores. Such a high SSA and relatively superabundant micropores will allow full contact of the electrolyte with the hard carbon surface and induce irreversible side reactions and then result in the formation of vast SEI layer and a low coulombic efficiency. Fortunately, the lower surface area of CNB will induce limited formation of solid electrolyte interphase (SEI) and increase the initial coulombic efficiency and cycle efficiency [15]. Besides, a quick rise of the  $\text{N}_2$  uptake at high pressure from 0.9 to 1.0 ( $P/P_0$ ) reflects large mesopores generated due to Fe species as template and graphitization catalysts. The micropore volume of CM and CNB is 0.29 and  $0.013 \text{ cm}^3/\text{g}$ , respectively. Figure S2a exhibits the detailed analysis of micropores distribution of CNB and CM. Compared with CM, CNB possess much

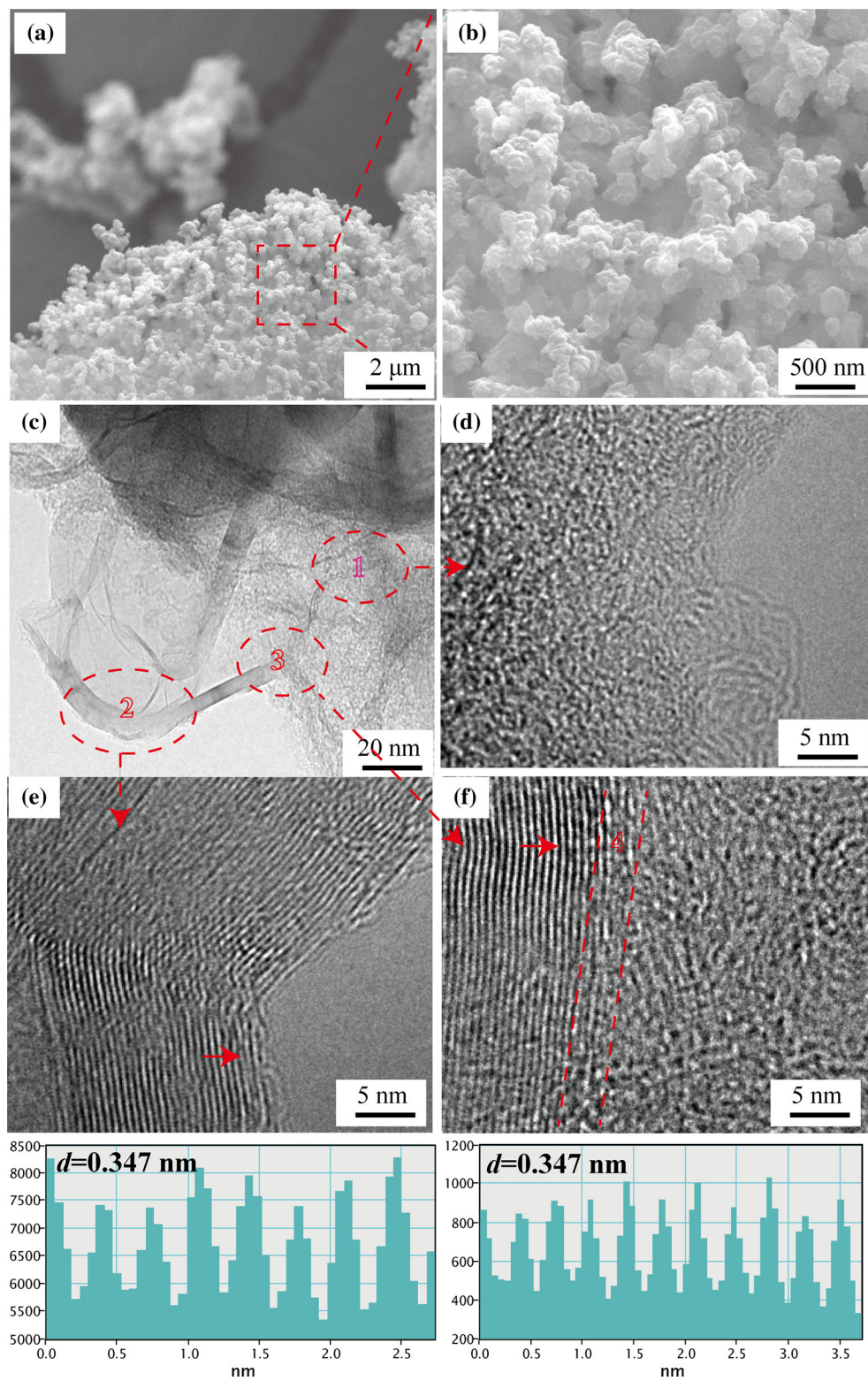


**Figure 3** The SEM images of CNB (a), (b), the HRTEM images of CNB (c), (d), (e), (f).

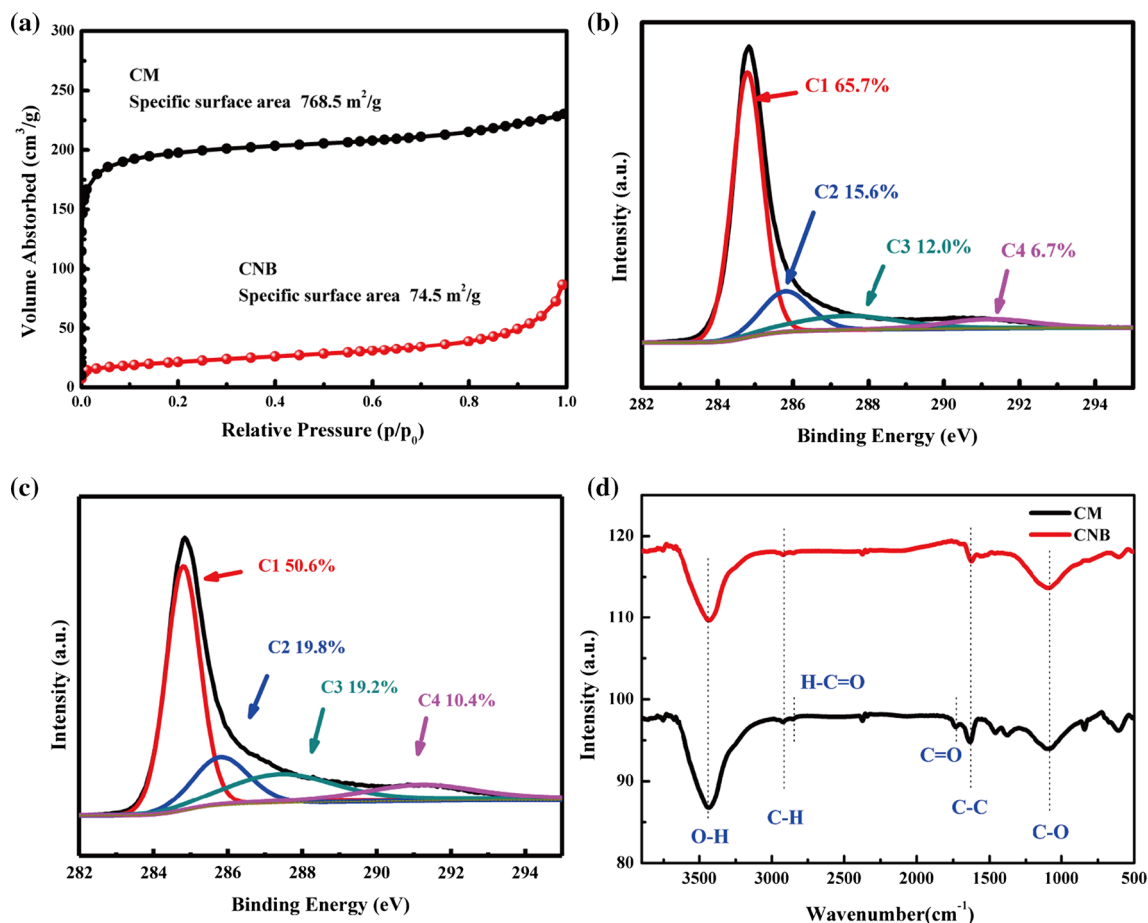


**Figure 4** a N<sub>2</sub> sorption isotherms for CNB and CM, b XPS C1s spectra of CNB, c XPS C1s spectra of CM, d FTIR spectra of CNB and CM.

less micropores. During the high-temperature carbonation process, Fe species scoured unstable structures in carbon matrix, consumed the polar intermediates of thermal decomposition of resin, hence decreased oxygen-containing functional groups as well as the stacking of *sp*<sup>3</sup> structures, broadened the micropores and increased graphene layers [32].

As displayed in Fig. S2b, element species are detected in the full survey scan of CNB and CM, including atomic concentrations of O 1s at 2.17 and 18.16%. Some reports demonstrate that superabundant oxygen will lead to vast irreversible sodium uptake [33]. As shown in Fig. 4b and c, the XPS spectra of C 1s were divided into four peaks at 284.8 eV (C1:C–C/C=C), 285.8 eV (C2:C–O), 287.4 eV (C3:C=O), 291.2 eV (C4:O=C–O). The *sp*<sup>2</sup> C content increases from 50.6% (CM) to 65.7% (CNB), which is in accord with the XRD, Raman and TEM results,

revealing a successful tailoring of graphitic nanostructures in hard carbon matrix for CNB.

Fourier-transform infrared (FTIR) spectra displayed in Fig. 4d demonstrate that both CNB and CM contain absorption peaks around 3439 cm<sup>-1</sup> pertaining to –OH stretching, 2921 cm<sup>-1</sup> of –C–H– bond and 1161 cm<sup>-1</sup> of –C–O– bond [19]. In addition, other absorption peaks at 1733, 2856 cm<sup>-1</sup> due to the C=O bond and H–C=O bond are observable in CM FTIR spectra, further confirming the existence of vast oxygen-containing groups in CM. Generally, the oxygen-containing functional groups will result in the surface redox reactions with sodium ions [6, 34, 35], and these oxygen-containing groups in carbon matrix may result in some side reactions [36] and lead to an adjective coulombic efficiency.

To understand the sodium storage behavior, CNB were packaged as working electrodes. Figure 5a depicts the initial five cyclic voltammetry curves from 3.0 to 0.01 V at a scan rate of 0.1 mV s<sup>-1</sup>. Three

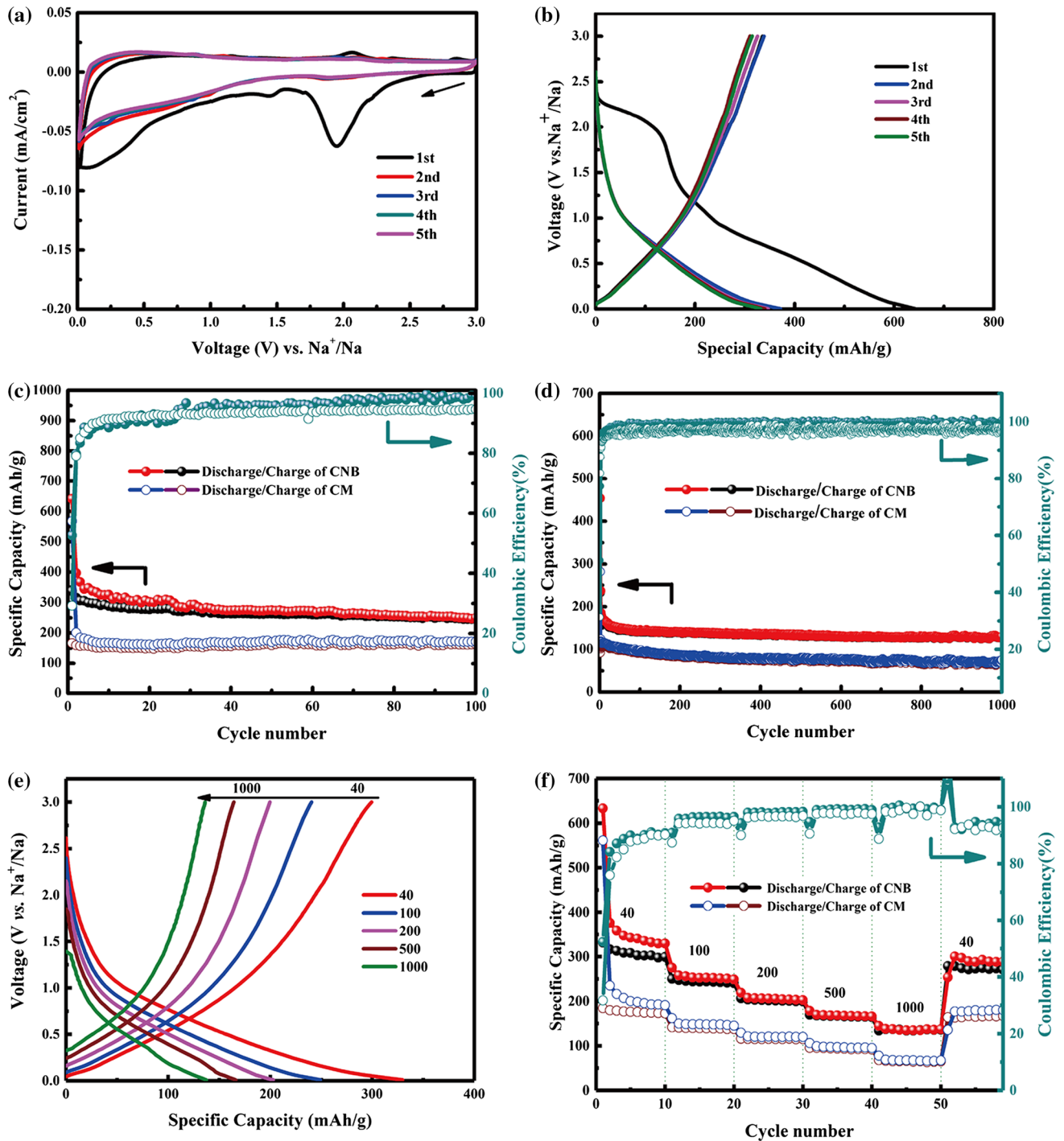


**Figure 5** Electrochemical characterization and battery performances of CNB and CM as anode material for SIBs. **a** Cyclic voltammetry curves of CNB. **b** Initial galvanostatic discharge/charge profiles of CNB at 50 mA g<sup>-1</sup>. **c** Cycle performance of CNB electrode at a current density of 50 mA g<sup>-1</sup>. **d** Cycle

performance of the electrode at a current density of 500 mA g<sup>-1</sup>. **e** Galvanostatic discharge/charge profiles of CNB at 40, 100, 200, 500, 1000 mA g<sup>-1</sup>. **f** Rate performance of CNB electrodes at current densities of 40, 100, 200, 500, 1000 mA g<sup>-1</sup>.

reduction peaks are clearly visible in the first cyclic voltammetry curve of CNB, indicating typical electrochemical behavior of carbons [2, 37]. Particularly,

the peaks at 2.0 and 1.5 V correspond to the irreversible reactions with surface functional groups as well as the formation of SEI. And the peak at 0.1 V

relates to the  $\text{Na}^+$  filling in CNB nanopores [38]. But, four CV curves almost coincide with each other and irreversible peaks disappear in the subsequent scans, indicating the excellent reversibility of  $\text{Na}^+$  storage for CNB electrode [39], which is much better than that of CM (Fig. S3).

The galvanostatic discharge/charge curves of CNB are displayed in Fig. 5b, and these curves show typical sodium storage behaviors of hard carbon with a short plateau region and a long sloping region [38]. The electrochemical curves of CNB are similar with each other from the second, demonstrating the excellent cycling stability. Different from the hard carbon microtubes derived from high-temperature-treated cotton [15], the CNB voltage profile dominating consists of the sloping region during cycling. According to the “house of card” model for amorphous carbon sodium storage [40], sodium ion insertion between the interlayers corresponds to the sloping region in the discharge curve, and the insertion of the sodium metal into the nanopores between randomly stacked layers makes great contribution to the low potential plateau region. Sodium chemical potential of the pore filling is close to 0 V, which is extremely dangerous in use. Based on similarity of CNB and typical carbons on carbon sources and carbon features, the contribution of the capacity according to mechanism of sodium ion storage into CNB is demonstrated as follows: the sloping region corresponds to the sodium storage performance in sodium insertion/desertion between expanded graphene layers.

As shown in Fig. 5c, the first discharge/charge specific capacities of CNB electrodes possess discharge/charge specific capacities of 641 and 337  $\text{mAh g}^{-1}$  with an initial coulombic efficiency (ICE) of 52.6% at 50  $\text{mA g}^{-1}$ , much higher than that of CM (568, 166  $\text{mAh g}^{-1}$ , 29%). The improved ICE can be attributed to the suppressed formation of SEI on the surface of CNB [20]. The discharge capacities are 337 and 249  $\text{mAh g}^{-1}$  at 2 and 100 cycles, respectively, exhibiting much superior cycling stability than those of CM. This is a remarkable capacity performance compared with high-temperature-treated hard carbon materials reported [19]. These research results reveal the remarkable superiority of tailoring graphitic nanostructures in hard carbon matrix with rational specific surface area.

Cycling performance at high rate is an important aspect to value the electrode materials of SIBs, which

is also a visualized method to evaluate the kinetic property of the CNB electrodes. And discharge/charge cycling at 500  $\text{mA g}^{-1}$  of CNB and CM was carried out. As displayed in Fig. 5d, at current of 500  $\text{mA g}^{-1}$ , the CNB electrodes deliver discharge/charge capacities of 453 and 232  $\text{mAh g}^{-1}$ , with an ICE of 51.2%. And the CNB electrodes exhibit excellent reversible specific capacities of 185 and 128  $\text{mAh g}^{-1}$  at 500  $\text{mA g}^{-1}$  at 2 and 1000 cycles, respectively; only 119 and 69  $\text{mAh g}^{-1}$  are for CM electrodes. Compared with the hard carbon electrodes derived from phenol formaldehyde resin [23] and hard carbon microtubes [15], CNB electrodes exhibit remarkable rate capability in half cells. Figure 5e shows the discharge/charge curves of CNB electrode at 40, 100, 200, 500, 1000  $\text{mA g}^{-1}$ , which corresponded well for all curves, indicating the well reliability of the carbon nanobroccoli hybrid in situ decorated with porous high graphitic nanostructures. Excellent electric conductivity is of greatest importance for electrode materials at high current density [41]. Tailoring expanded graphitic nanostructures in hard carbons can greatly promote charge transfer and hence decrease charge transfer impedance [41, 42]. Figure 5f displays the sodium storage performances of the CNB electrodes, which deliver specific capacities of 331, 250, 206, 169, 137  $\text{mAh g}^{-1}$  at current densities of 40, 100, 200, 500, 1000  $\text{mA g}^{-1}$ . When the current density is reset to 40  $\text{mA g}^{-1}$ , 278  $\text{mAh g}^{-1}$  can be retrained. Table 1 shows the comparison between the CNB and typical carbon anodes for SIBs reported [1, 3, 4, 9, 10, 21, 23, 37, 38], suggesting the excellent sodium storage of CNB. Among scalable carbon precursor-derived hard carbons, rare materials exhibited comparably accomplished durable high capabilities, suggesting the superiority of the smart tailored structure of CNB hybrid. All these results above demonstrate high initial coulombic efficiency, excellent specific capacity and high-rate capability of CNB for efficient and fast sodium storage.

To better understand the superiority of CNB electrodes, electrochemical impedance spectroscopy (EIS) measurements of CNB and CM electrodes were carried out after the first cycle (and CNB electrode after five cycles) at 3.0 V. As displayed in Fig. 6a, all Nyquist plots exhibit an oblique line in low-frequency region and a depressed semicircle in high-/medium-frequency region, which reflect the diffusion of  $\text{Na}^+$  and charge transfer resistance in electrode material [43, 44]. It is clearly observed that the



**Table 1** Comparison of the performances of the SIBs based on the CNB electrode with those of other typically carbon electrode materials

	Mass loading (mg cm <sup>-2</sup> )	Rate capacity	Initial coulombic efficiency (%)	Ref.
CNB	1.02	337 mA h g <sup>-1</sup> at 50 mA g <sup>-1</sup> 210 mA h g <sup>-1</sup> at 500 mA g <sup>-1</sup> (1000 cycles)	52.6	This work
Biomass-derived hard carbon	2.0	139 mA h g <sup>-1</sup> at 1 A g <sup>-1</sup> 314 mA h g <sup>-1</sup> at 50 mA g <sup>-1</sup> 151 mA h g <sup>-1</sup> at 500 mA g <sup>-1</sup> 118 mA h g <sup>-1</sup> at 1 A g <sup>-1</sup>	27	[38]
Nitrogen-doped carbon sheets		212 mA h g <sup>-1</sup> at 100 mA g <sup>-1</sup> 129 mA h g <sup>-1</sup> at 100 mA g <sup>-1</sup> 113 mA h g <sup>-1</sup> at 100 mA g <sup>-1</sup>	26	[2]
MgO-templated carbon		120 mA h g <sup>-1</sup> at 90 mA g <sup>-1</sup> 90 mA h g <sup>-1</sup> at 450 mA g <sup>-1</sup> 85 mA h g <sup>-1</sup> at 900 mA g <sup>-1</sup>	< 30	[4]
Microporous hard carbon		245 mA h g <sup>-1</sup> at 100 mA g <sup>-1</sup> 150 mA h g <sup>-1</sup> at 500 mA g <sup>-1</sup> 100 mA h g <sup>-1</sup> at 1000 mA g <sup>-1</sup>	47	[9]
Hollow carbon nanospheres		223 mA h g <sup>-1</sup> at 50 mA g <sup>-1</sup> 142 mA h g <sup>-1</sup> at 500 mA g <sup>-1</sup> 120 mA h g <sup>-1</sup> at 1000 mA g <sup>-1</sup>	42	[21]
Nitrogen-doped carbon microspheres	2.0	154 mA h g <sup>-1</sup> at 1000 mA g <sup>-1</sup>	30	[23]
Nitrogen-containing hollow carbon microspheres	0.55	303 mA h g <sup>-1</sup> at 50 mA g <sup>-1</sup> 163 mA h g <sup>-1</sup> at 200 mA g <sup>-1</sup> 181 mA h g <sup>-1</sup> at 500 mA g <sup>-1</sup>	24	[37]
Expanded graphite	0.5	280 mA h g <sup>-1</sup> at 20 mA g <sup>-1</sup> 91 mA h g <sup>-1</sup> at 200 mA g <sup>-1</sup>	49	[1]

diameters of semicircles for CNB electrode are much less than that of CM electrode, demonstrating the less charge transfer resistance ( $R_{ct1}$  of CNB at 187  $\Omega$ ,  $R_{ct5}$  of CNB at 103  $\Omega$ ,  $R_{ct1}$  of CM at 597  $\Omega$ ), suggesting faster charge transfer capability at electrode–electrolyte interface [42]. Upon the cycling, irreversible reaction of sodium ion with surface functional groups was declining, and steady solid–electrolyte interphase (SEI) also generated on the carbon anode electrode [1, 3]; as a result, the carbon anode electrode delivered decreasing charge transfer resistance and became steady. Additionally, based on the Warburg factor related to  $Z_{Re}$ , the Na<sup>+</sup> diffusion coefficient in the electrodes can be quantified according to the following equations [45, 46]:

$$Z_{Re} = R_s + R_{ct} + \sigma\omega^{-1/2} \tag{2}$$

where  $R_s$  is the resistance between electrode and electrolyte.

$$D = \frac{R^2 T^2}{2A^2 n^4 F^4 C^2 \sigma^2} \tag{3}$$

where  $n$  is the number of transferred electrons,  $T$  is absolute temperature,  $R$  is gas constant,  $A$  is active surface area of electrodes,  $C$  is the concentration of Na<sup>+</sup>,  $F$  is faraday constant,  $R_{ct}$  is charge transfer resistance and  $\sigma$  is the Warburg factor.

Figure 6b displays the relationship between  $Z_{Re}$  and  $\omega$  of the CNB electrodes and CM electrodes in the low-frequency region. As calculated based on Eqs. (2, 3),  $\sigma$  value of CNB electrodes is smaller than that of CM fresh electrode (Fig. 6c). Impressively, CNB electrodes possess much higher Na<sup>+</sup> diffusion coefficient ( $5.9 \times 10^{-10}$  cm<sup>2</sup> s<sup>-1</sup>), which is about 125 times than that of CM electrodes ( $4.7 \times 10^{-12}$  cm<sup>2</sup> s<sup>-1</sup>), demonstrating an superior sodium ions diffusion kinetics in CNB electrode. Due to the in situ tailored porous graphitic nanostructures in hard carbons, CNB electrodes exhibit less charge transfer resistance as well as excellent sodium ion diffusion kinetics and then successfully achieve superior cycling stability and excellent rate performance [14, 47–55].

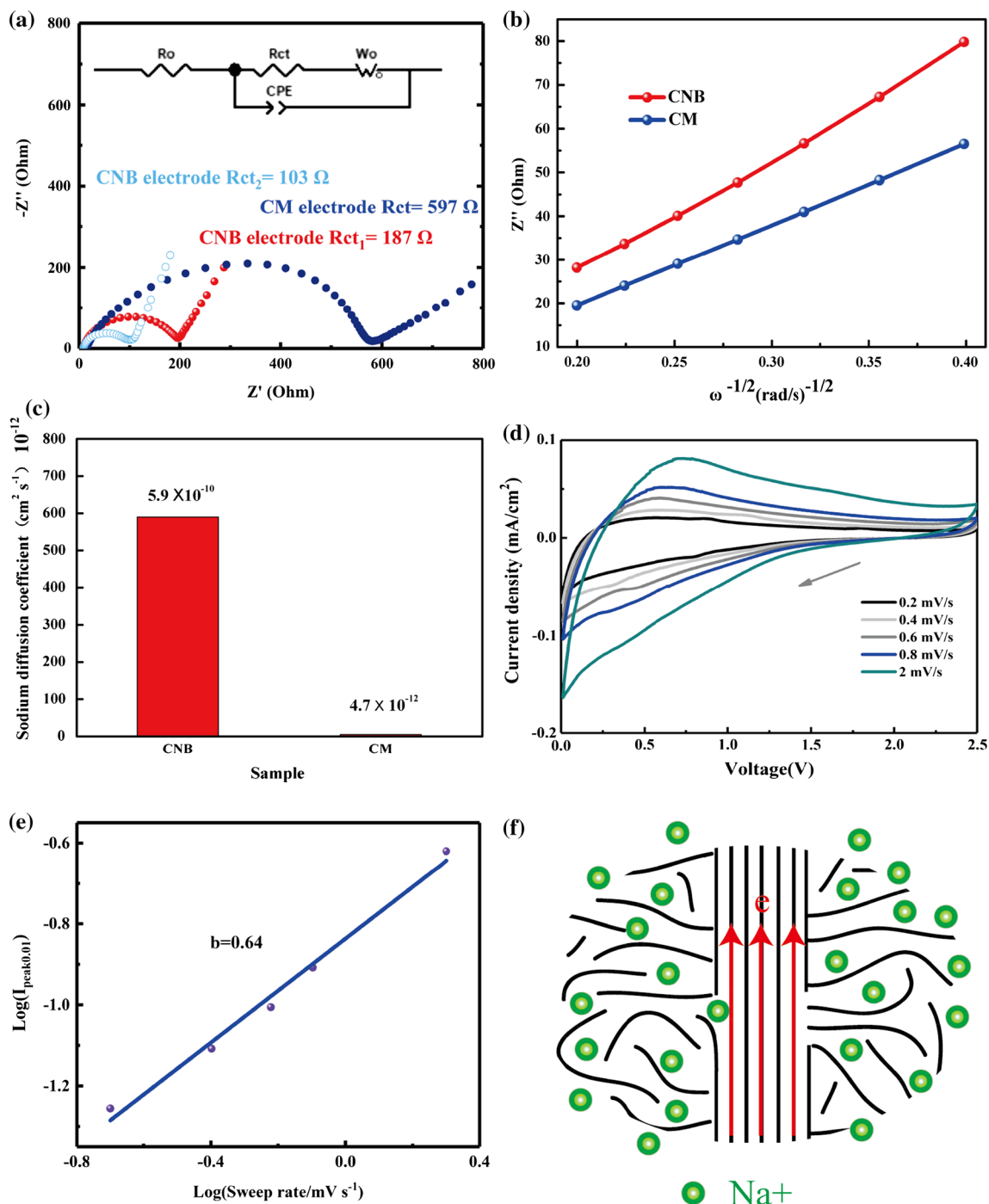


**Figure 6** **a** Electrochemical impedance spectra of the CNB and CM electrodes at  $50 \text{ mA g}^{-1}$  first cycle, electrochemical impedance spectra of the CNB electrodes at  $50 \text{ mA g}^{-1}$  after five cycles. **b** The relationship between  $Z_{\text{Re}}$  and  $\omega^{-1/2}$  of CNB and CM fresh electrode. **c** Sodium diffusion coefficients of CNB and CM fresh electrode. **d** CV curves of the CNB electrode at different scan rates. **e** Relationship between  $\log i$  and  $\log v$  plots for the anodic

sweeps of CV. **f** Schematic illustration of CNB electrodes for sodium storage processes. Expanded graphitic nanostructures in situ decorated on turbostratic structure hard carbon guarantees fast electron transport, while well-reserved amorphous hard carbon tailored with graphitic nanostructures facilitates  $\text{Na}^+$  diffusion and de-intercalation.

To further understand the sodium storage mechanism of CNB electrodes and electrochemical process in SIB, CV tests of CNB electrodes were conducted at varied scan rates from 0.2 to 2 mV s<sup>-1</sup>, and these results are displayed in Fig. 6d. In the circumstances, the current response at a specific voltage can be identified as the combination of the diffusion-controlled contribution ( $k_2v^{1/2}$ ) and the capacitive contribution ( $k_1v$ ). Meanwhile, it can be assumed that the response current value has an exponential relationship with the CV scan rate [50, 51].

$$i(V) = k_1v + k_2v^{1/2} = av^b \quad (4)$$

$$\log i(V) = b \log v + \log a \quad (5)$$

where  $v$  is the CV scan rate,  $k_1$ ,  $k_2$ , and  $a$  are constants and  $b$  is a value ranging from 1 (capacitive contribution) to 0.5 (diffusion-controlled contribution).

Based on Eqs. (4) and (5), the  $b$  value can be calculated to be 0.64 (Fig. 6e), and the value represents a relatively low capacitive contribution for the CNB electrodes, demonstrating the electrochemistry process of sodium storage behavior in diffusion control [51, 54].

As illustrated in Fig. 6f, expanded graphitic nanostructures in situ decorated on amorphous structure in hard carbon guarantees fast electron transport, while well-reserved amorphous hard carbons tailored with graphitic nanostructures facilitates Na<sup>+</sup> diffusion and de-intercalation. Meanwhile, the excellent sodium storage capacities of CNB electrodes can be attributed to the unique characteristics as followed. (1) Catalytic graphitization can be achieved at low temperature, which is benefit for preserving the amorphous structure of hard carbons. The unique architecture exhibits high-sodium storage specific capacity. (2) Rational specific surface area will result in limited formation of SEI on electrodes surface. (3) The tailored expanded graphitic nanostructure in the hard carbon matrix can promote rapid charge transfer, reduce the charge transfer resistance and hence improve the rate performance for sodium storage. (4) The unique architecture exhibits superior sodium ion diffusion kinetics. These above results strongly suggest that the CNB are a greatly promising anode material for SIBs.

## Conclusion

In summary, amorphous hard carbons tailored with expanded graphitic structures have been successfully synthesized by spontaneous growth and catalytic graphitization. The resin-derived hard carbons are rational, scalable and economically feasible. CNB possess amorphous structures, ordered graphitic structures as well as rational specific surface area (74.5 m<sup>2</sup>g<sup>-1</sup>) with the template as well as the catalytic graphitization of Fe species, and then result in limited formation of SEI, less irreversible capacity, enhanced electronic conductivity and decreased charge transfer resistance and superior sodium ion diffusion kinetics. The unique constructions achieved demonstrate superior specific capacity of 337 mAh g<sup>-1</sup> at 50 mA g<sup>-1</sup> with much improved ICE of 52.6%, and excellent cycling stability at 210 mAh g<sup>-1</sup> at 500 mA g<sup>-1</sup> at 1000 cycles as well as great high-rate performance at 139 mAh g<sup>-1</sup> at 1000 mA g<sup>-1</sup>, much higher than those of traditional hard carbon monolith. The CNB hold great potential as anode materials for practical SIBs. In addition, such architectures provide a promising structural platform for the fabrication of amorphous carbon decorated with ordered nanostructures possessing excellent electronic and ion conductivity in other energy storage systems, such as supercapacitor, lithium-ion batteries and Li-S batteries.

## Acknowledgements

The authors thank the financial support of the National Natural Science Foundation of China (Grant No. 51674297) and the Natural Science Foundation of Hunan Province (Grant No. 2016JJ2137). The authors thank the financial support of the Basic Research Program of Shenzhen, China (Grant No. JCYJ20170307140332076).

## Compliance with ethical standards

**Conflicts of interest** The authors declare no competing financial interest.

**Electronic supplementary material:** The online version of this article (<https://doi.org/10.1007/>

s10853-018-2295-3) contains supplementary material, which is available to authorized users.

## References

- [1] Wen Y, He K, Zhu Y, Han F, Xu Y, Matsuda I, Ishii Y, Cumings J, Wang C (2014) Expanded graphite as superior anode for sodium-ion batteries. *Nat Commun* 5:4033–4040
- [2] Wang S, Xia L, Yu L, Zhang L, Wang H, Lou XWD (2016) Free-standing nitrogen-doped carbon nanofiber films: integrated electrodes for sodium-ion batteries with ultralong cycle life and superior rate capability. *Adv Energy Mater* 6:1502217
- [3] Cao Y, Xiao L, Sushko ML, Wang W, Schwenzler B, Xiao J, Nie Z, Saraf LV, Yang Z, Liu J (2012) Sodium ion insertion in hollow carbon nanowires for battery applications. *Nano Lett* 12:3783–3787
- [4] Yang F, Zhang Z, Du K, Zhao X, Chen W, Lai Y, Li J (2015) Dopamine derived nitrogen-doped carbon sheets as anode materials for high-performance sodium ion batteries. *Carbon* 91:88–95
- [5] Zhu J, Chen C, Lu Y, Ge Y, Jiang H, Fu K, Zhang X (2015) Nitrogen-doped carbon nanofibers derived from polyacrylonitrile for use as anode material in sodium-ion batteries. *Carbon* 94:189–195
- [6] Gaddam RR, Yang D, Narayan R, Raju K, Kumar NA, Zhao XS (2016) Biomass derived carbon nanoparticle as anodes for high performance sodium and lithium ion batteries. *Nano Energy* 26:346–352
- [7] Kim H, Hong J, Park YU, Kim J, Hwang I, Kang K (2015) Sodium storage behavior in natural graphite using ether-based electrolyte systems. *Adv Funct Mater* 25:534–541
- [8] Zhang SW, Lv W, Luo C, You CH, Zhang J, Pan ZZ, Kang FY, Yang QH (2016) Commercial carbon molecular sieves as a high performance anode for sodium-ion batteries. *Energy Storage Mater* 3:18–23
- [9] Li D, Zhang L, Chen H, Ding LX, Wang S, Wang H (2015) Nitrogen-doped bamboo-like carbon nanotubes: promising anode materials for sodium-ion batteries. *Chem Commun* 51:16045–16048
- [10] Tang K, Fu L, White RJ, Yu L, Titirici M-M, Antonietti M, Maier J (2012) Hollow carbon nanospheres with superior rate capability for sodium-based batteries. *Adv Energy Mater* 2:873–877
- [11] Väli R, Jänes A, Thomberg T, Lust E (2016) D-Glucose derived nanospheric hard carbon electrodes for room-temperature sodium-ion batteries. *J Electrochem Soc* 163:A1619–A1626
- [12] Li Y, Xu S, Wu X, Yu J, Wang Y, Hu YS, Li H, Chen L, Huang X (2015) Amorphous monodispersed hard carbon micro-spherules derived from biomass as a high performance negative electrode material for sodium-ion batteries. *J Mater Chem A* 3:71–77
- [13] Hong KL, Qie L, Zeng R, Yi ZQ, Zhang W, Wang D, Yin W, Wu C, Fan QJ, Zhang WX, Huang YH (2014) Biomass derived hard carbon used as a high performance anode material for sodium ion batteries. *J Mater Chem A* 2:12733–12738
- [14] Li Y, Hu YS, Qi X, Rong X, Li H, Huang X, Chen L (2016) Advanced sodium-ion batteries using superior low cost pyrolyzed anthracite anode: towards practical applications. *Energy Storage Mater* 5:191–197
- [15] Li Y, Hu YS, Titirici MM, Chen L, Huang X (2016) Hard carbon microtubes made from renewable cotton as high-performance anode material for sodium-ion batteries. *Adv Energy Mater* 6:1600659
- [16] Shen F, Luo W, Dai J, Yao Y, Zhu M, Hitz E, Tang Y, Chen Y, Sprenkle VL, Li X, Hu L (2016) Ultra-thick, low-tortuosity, and mesoporous wood carbon anode for high-performance sodium-ion batteries. *Adv Energy Mater* 6:1600377
- [17] Zheng P, Liu T, Guo S (2016) Micro-nano structure hard carbon as a high performance anode material for sodium-ion batteries. *Sci Rep* 6:35620
- [18] Luo W, Shen F, Bommier C, Zhu H, Ji X, Hu L (2016) Na-ion battery anodes: materials and electrochemistry. *Acc Chem Res* 49:231–240
- [19] Li Y, Paranthaman MP, Akato K, Naskar AK, Levine AM, Lee RJ, Kim SO, Zhang J, Dai S, Manthiram A (2016) Tire-derived carbon composite anodes for sodium-ion batteries. *J Power Sources* 316:232–238
- [20] Liu P, Li Y, Hu YS, Li H, Chen L, Huang X (2016) A waste biomass derived hard carbon as a high-performance anode material for sodium-ion batteries. *J Mater Chem A* 4:13046–13052
- [21] Kado Y, Soneda Y (2016) MgO-templated carbon as a negative electrode material for Na-ion capacitors. *J Phys Chem Solid* 99:167–172
- [22] Elkhatat AM, Al-Muhtaseb SA (2011) Advances in tailoring resorcinol-formaldehyde organic and carbon gels. *Adv Mater* 23:2887–2903
- [23] Yu ZL, Xin S, You Y, Yu L, Lin Y, Xu DW, Qiao C, Huang ZH, Yang N, Yu SH, Goodenough JB (2016) Ion-catalyzed synthesis of microporous hard carbon embedded with expanded nanographite for enhanced lithium/sodium storage. *J Am Chem Soc* 138:14915–14922
- [24] Yu ZL, Li GC, Fechner N, Yang N, Ma ZY, Wang X, Antonietti M, Yu SH (2016) Polymerization under

- hypersaline conditions: a robust route to phenolic polymer-derived carbon aerogels. *Angew Chem Int Edit* 128:14843–14847
- [25] Nelson KM, Mahurin SM, Mayes RT, Williamson B, Teague CM, Binder AJ, Baggetto L, Veith GM, Dai S (2016) Preparation and CO<sub>2</sub> adsorption properties of soft-templated mesoporous carbons derived from chestnut tannin precursors. *Micro Meso Mater* 222:94–103
- [26] Tejado A, Pena C, Labidi J, Echeverria JM, Mondragon I (2007) Physico-chemical characterization of lignins from different sources for use in phenol-formaldehyde resin synthesis. *Bio Tech* 98:1655–1663
- [27] Shi L, Chen K, Du R, Bachmatiuk A, Rummeli MH, Priyadarshi MK, Zhang Y, Manivannan A, Liu Z (2015) Direct synthesis of few-layer graphene on NaCl crystals. *Small* 11:6302–6308
- [28] Lu AH, Li WC, Hao GP, Spliethoff B, Bongard HJ, Schaack BB, Schuth F (2010) Easy synthesis of hollow polymer, carbon, and graphitized microspheres. *Angew Chem Int Edit* 49:1615–1618
- [29] Dong Y, Yu M, Wang Z, Liu Y, Wang X, Zhao Z, Qiu J (2016) A top-down strategy toward 3D carbon nanosheet frameworks decorated with hollow nanostructures for superior lithium storage. *Adv Funct Mater* 26:7590–7598
- [30] Campos-Roldan CA, Ramos-Sanchez G, Gonzalez-Huerta RG, Vargas Garcia JR, Balbuena PB, Alonso-vante N (2016) Influence of *sp*(3)-*sp*(2) carbon nanodomains on metal/support interaction, catalyst durability, and catalytic activity for the oxygen reduction reaction. *ACS Appl Mater Interfaces* 8:23260–23269
- [31] Yan Y, Yin YX, Guo YG, Wan LJ (2014) A sandwich-like hierarchically porous carbon/graphene composite as a high-performance anode material for sodium-ion batteries. *Adv Energy Mater* 4:1301584
- [32] Su D, Cortie M, Wang G (2016) Fabrication of N-doped graphene-carbon nanotube hybrids from prussian blue for lithium-sulfur batteries. *Adv Energy Mater* 7:1602014
- [33] Dou X, Hasa I, Hekmatfar M, Diemant T, Behm RJ, Buchholz D, Passerini S (2017) Pectin, hemicellulose or lignin? Impact of the biowaste source on the performance of hard carbons for sodium ion batteries. *Chemsuschem* 10:2668–2676. <https://doi.org/10.1002/cssc.201700628>
- [34] Park Y, Shin DS, Woo SH, Choi NS, Shin KH, Oh SM, Lee KT, Hong SY (2012) Sodium terephthalate as an organic anode material for sodium ion batteries. *Adv Mater* 24:3562–3567
- [35] Wang H, Yu W, Mao N, Shi J, Liu W (2016) Effect of surface modification on high-surface-area carbon nanosheets anode in sodium ion battery. *Micro Meso Mater* 227:1–8
- [36] Lotfabad EM, Ding J, Cui K, Kohandehghan A, Kalisvaart WP, Hazelton M, Mitlin D (2014) High-density sodium and lithium ion battery anodes from banana peels. *ACS Nano* 8:7115–7129
- [37] Qu Y, Zhang Z, Du K, Chen W, Lai Y, Liu Y, Li J (2016) Synthesis of nitrogen-containing hollow carbon microspheres by a modified template method as anodes for advanced sodium-ion batteries. *Carbon* 105:103–112
- [38] Ou J, Yang L, Zhang Z, Xi X (2017) Nitrogen-doped porous carbon derived from horn as an advanced anode material for sodium ion batteries. *Micro Meso Mater* 237:23–30
- [39] Luo XF, Yang CH, Chang JK (2015) Correlations between electrochemical Na<sup>+</sup> storage properties and physicochemical characteristics of holey graphene nanosheets. *J Mater Chem A* 3:17282–17289
- [40] Stevens DA, Dahn JR (2000) High capacity anode materials for rechargeable sodium-ion batteries. *J Electrochem Soc* 147:1271–1273
- [41] Peng XX, Lu YQ, Zhou LL, Sheng T, Shen SY, Liao HG, Huang L, Li JT, Sun SG (2017) Graphitized porous carbon materials with high sulfur loading for lithium-sulfur batteries. *Nano Energy* 32:503–510
- [42] Zhang Y, Chen L, Meng Y, Xie J, Guo Y, Xiao D (2016) Lithium and sodium storage in highly ordered mesoporous nitrogen-doped carbons derived from honey. *J Power Sources* 335:20–30
- [43] Li Z, Huang Y, Yuan L, Hao Z, Huang Y (2015) Status and prospects in sulfur-carbon composites as cathode materials for rechargeable lithium-sulfur batteries. *Carbon* 92:41–63
- [44] Wang HL, Shi ZQ, Jin J, Chong C-B, Wang CY (2015) Properties and sodium insertion behavior of phenolic resin-based hard carbon microspheres obtained by a hydrothermal method. *J Electroanal Chem* 755:87–91
- [45] Sun Y, Tang J, Zhang K, Yuan J, Li J, Zhu DM, Ozawa K, Qin LC (2017) Comparison of reduction products from graphite oxide and graphene oxide for anode applications in lithium-ion batteries and sodium-ion batteries. *Nanoscale* 9:2585–2595
- [46] Lv X, Song J, Lai Y, Fang J, Li J, Zhang Z (2016) Ultrafine nanoparticles assembled Mo<sub>2</sub>C nanoplates as promising anode materials for sodium ion batteries with excellent performance. *J Energy Storage* 8:205–211
- [47] Zhang W, Jiang X, Wang X, Kaneti YV, Chen Y, Liu J, Jiang JS, Yamauchi Y, Hu M (2017) Spontaneous weaving of graphitic carbon networks synthesized by pyrolysis of ZIF crystals. *Angew Chem Int Edit* 56:8435–8440. <https://doi.org/10.1002/anie.201701252>
- [48] Xiong W, Wang Z, Zhang J, Shang C, Yang M, He L, Lu Z (2017) Hierarchical ball-in-ball structured nitrogen-doped

- carbon microspheres as high performance anode for sodium-ion batteries. *Energy Storage Mater* 7:229–235
- [49] Liu Y, Zhang N, Liu X, Chen C, Fan LZ, Jiao L (2017) Red phosphorus nanoparticles embedded in porous N-doped carbon nanofibers as high-performance anode for sodium-ion batteries. *Energy Storage Mater* 9:170–178
- [50] Zou G, Hou H, Zhao G, Huang Z, Ge P, Ji X (2017) Preparation of S/N-codoped carbon nanosheets with tunable interlayer distance for high-rate sodium-ion batteries. *Green Chem* 19:4622–4632
- [51] Xia X, Chao D, Zhang Y, Zhan J, Zhong Y, Wang X, Fan HJ (2016) Generic synthesis of carbon nanotube branches on metal oxide arrays exhibiting stable high-rate and long-cycle sodium ion storage. *Small* 12:3048–3058
- [52] Zhang L, Wang M, Lai Y, Li X (2018) Oil/molten salt interfacial synthesis of hybrid thin carbon nanostructures and their composites. *J Mater Chem A* 6:4988–4996. <https://doi.org/10.1039/C7TA10692K>
- [53] Balogun MS, Luo Y, Qiu W, Liu P, Tong Y (2016) A review of carbon materials and their composites with alloy metals for sodium ion battery anodes. *Carbon* 98:162–178
- [54] Chen Y, Li J, Lai Y, Xu M, Li J, Wang P, Zhang Z (2018) Engineering anisotropically curved N-doped carbon nanosheets with recyclable binary flux to achieve superior sodium ion storage. *Chemsuschem*. <https://doi.org/10.1002/cssc.201702436>
- [55] Balogun MS, Qiu W, Lyu F, Luo Y, Meng H, Li J, Tong Y (2016) All-flexible lithium ion battery based on thermally-etched porous carbon cloth anode and cathode. *Nano Energy* 26:446–455